LAWRENCE
LIVERMORE
NATIONAL
LABORATORY

LLNL-JRNL-667212

Location of High-Frequency P-wave Microseismic Noise in the Pacific Ocean Using Multiple Small Aperture Arrays

M. L. Pyle, K. D. Koper, G. G. Euler, R. Burlacu

February 12, 2015

Geophysical Research Letters

Disclaimer

Location of High-Frequency P-wave Microseismic Noise in the Pacific Ocean Using Multiple Small Aperture Arrays

Moira L. Pyle[1], Keith D. Koper[2], Garrett G. Euler[3], and Relu Burlacu[2]

[1]Lawrence Livermore National Laboratory

7000 East Ave.

Livermore, CA 94550

pyle4@llnl.gov

925-423-3820

[2]Department of Geology and Geophysics, University of Utah, Salt Lake City, UT, USA

[3]Los Alamos National Laboratory, Los Alamos, NM, USA

Prepared for submission to Geophysical Research Letters

LLNL-JRNL-667212

LA-UR-15-21040

Abstract

We investigate source locations of P-wave microseisms within a narrow frequency band (0.67–1.33 Hz) that is significantly higher than the classic microseism band (~0.05–0.3 Hz). Employing a back-projection method, we analyze data recorded during January 2010 from five International Monitoring System arrays that border the Pacific Ocean. We develop a ranking scheme that allows us to combine beam power from multiple arrays to obtain robust locations of the microseisms. Some individual arrays exhibit a strong regional component, but results from the combination of all arrays show high frequency P-wave energy emanating from the North Pacific basin, in general agreement with previous observations in the double-frequency (DF) microseism band (~0.1–0.3 Hz). This suggests that the North Pacific source of ambient P noise is broadband and that the wave-wave interaction model invoked to explain DF microseisms is likely valid at shorter periods.

1. Introduction

The existence of coherent energy in the microseismic noise spectrum has been recognized for a long time [e.g., *Ebeling*, 2012], but the role of this energy in geophysical research is rapidly expanding. Applications of seismic noise are wide-ranging and include Earth imaging techniques such as velocity tomography [e.g., *Shapiro et al.*, 2005] and attenuation structure estimation [e.g., *Lawrence and Prieto*, 2011], ground motion prediction for hazard estimation [e.g., *Denolle et al.*, 2013], monitoring temporal changes in Earth structure [e.g., *Brenguier et al.*, 2008], studying historic climate and sea states [e.g., *Aster et al.*, 2008], and storm tracking [e.g., *Gerstoft et al.*, 2006]. As the uses expand, it is desirable to obtain a more complete understanding of the generation and source locations of microseisms.

Microseismic energy is strongest in the frequency band from ~0.05–0.2 Hz. Single frequency microseisms [*Hasselmann*, 1963; *Traer and Gerstoft*, 2014] have a peak at ~0.07 Hz and travel dominantly as Rayleigh and Love waves. Double frequency (DF) microseisms are more energetic, with a peak at ~0.14 Hz, and contain both surface and body wave components [e.g., *Haubrich and McCamy*, 1969]. DF microseisms are produced by the interaction of opposing ocean surface gravity waves, which generate pressure fluctuations that excite seismic waves at the sea floor [e.g., *Longuet-Higgins*, 1950; *Hasselmann*, 1963; *Ardhuin and Herbers*, 2013]. Microseismic surface wave energy dominates the DF frequency band, but body waves are commonly observed [e.g., *Boué et al.*, 2014; *Euler et al.*, 2014; *Gerstoft et al.*, 2006, 2008; *Koper and de Foy*, 2008; *Landès et al.*, 2010; *Obrebski et al.*, 2013; *Poli et al.*, 2012; *Roux et al.*, 2005; *Toksöz and Lacoss*, 1968; *Zhang et al.*, 2010], and recent modeling work has shown that the generation of these body waves is distinct from that of surface waves [*Ardhuin and Herbers*, 2013; *Obrebski et al.*, 2013].

Most studies of body wave DF microseisms have concentrated on the most energetic frequency range (~0.1–0.3 Hz) in part because the arrays used in such studies have apertures that are too large for higher frequencies to be coherent across the array. However, recent analysis at smaller aperture arrays has shown that higher frequency body wave energy can be observed globally and consistently [*Koper et al.*, 2010; *Reading et al.*, 2014; *Zhang et al.*, 2009], although the location methods at these frequencies have generally been less sophisticated than those at lower frequencies. Here we extend the investigation of the high frequency P-wave microseismic noise in the Pacific Ocean using arrays from the International Monitoring System (IMS). Figure 1 shows the location of these arrays along with previous P-wave DF microseism source locations in the North Pacific Ocean. By combining multiple arrays we obtain a robust look at high frequency noise generation in this same region.

2. Data

To investigate possible source locations for the high-frequency body wave noise energy, we use data from seismic array stations of the International Monitoring System (IMS) that surround the Pacific Ocean. We select five arrays (ASAR, CMAR, ILAR, KSRS, and YKA) that have previously been shown to record significant P-wave noise energy [*Koper et al.*, 2010]. Data from ASAR, ILAR, and YKA are freely available from the IRIS DMC, however, data from CMAR and KSRS are not available to the general public and only a limited dataset was available to the authors at the time of this study. As a result, we examine one month of data during January 2010 with all five arrays.

The arrays consist of 15 to 21 short period, vertical component seismometers with apertures ranging from ~10–25 km (Figure 1). The small aperture of the arrays allows for the

coherency of high frequency signals at all components. Array response functions indicate that the best resolution corresponds to the frequency band of ~0.33-1.33 Hz (Figure S1). At lower frequencies, the size of the central lobe increases, making it more difficult to distinguish between lower apparent velocities of surface waves and higher velocities expected for body waves. At higher frequencies, the central lobe becomes tighter with better distinction of high apparent velocities, but grating lobes become stronger making analysis increasingly difficult. We select the 0.67–1.33 Hz band to consider high frequency energy while staying within the optimal resolution capabilities of the arrays.

3. Methods

3.1 Microseismic energy back-projection

We apply a back-projection method similar to that used for rupture imaging by *Xu et al.* [2009] to perform a grid search for possible source locations. Data from each array are back-projected through a reference 1D velocity model to points on a grid within the distance range of 0°–105°, allowing for the propagation of both regional and teleseismic P-waves, but excluding core-diffracted and core-traversing phases. Each array is processed independently, but we use a common, global grid of points so that the arrays can later be combined. Grid spacing is approximately 200 km (Figure S2). For any beam, we require that at least 75% of the array stations have returned data, in order to prevent bias from grid points and time windows using only a small fraction of the stations. We do not explicitly remove earthquakes from the data; however, we find back-projected energy generally concentrates away from the earthquake-prone areas, indicating that our results are primarily sensitive to coherent microseismic signals and not to earthquakes.

105 The data are processed in hour-long segments. We remove the mean and trend and filter
106 each trace from 0.67–1.33 Hz. For each assumed source time and grid point, we cut a 10-second
107 time window from each array component corresponding to the P-wave arrival time predicted by
108 ak135 [*Kennett et al.*, 1995]. Windows are normalized and tapered so that power is based more
109 on coherency than amplitude. We form 4^{th} root beams [e.g., *Muirhead and Datt,* 1976], which
110 mitigates the effects of anomalous individual waveforms and enhances coherent energy, and
111 measure the beam power in a root-mean-square sense. Beam power is calculated at every point
112 on the grid within the appropriate distance range, and the process is repeated for the next source
113 time. We assume a new time source every 5 seconds and use 10-second windows to capture as
114 many potential sources of coherent energy as possible. The 50% overlap helps to account for the
115 window tapers. We note that even with drastically different time windows (for example, 10
116 minutes instead of 10 seconds) we obtain similar results, suggesting that the P-wave
117 microseismic noise field is quite stationary.

118 **3.2 Array combination**

119 Once beam powers have been calculated for individual arrays, we seek to average the
120 results from all arrays to obtain better constraints on source locations; however, the combination
121 of multiple arrays is not straightforward due to large variations in maximum powers and the
122 range of power among the arrays, as well as differing array responses. If a simple average of the
123 powers from all arrays is performed, the array with the highest power dominates the average.
124 Figure 2a shows the maximum powers during a quiet hour for all of the individual arrays, as well
125 as the maximum average power in each window obtained by calculating the mean over the entire
126 grid from all five arrays. In this case, the average power is nearly indistinguishable from the
127 power at ILAR. Linear normalization techniques preserve this discrepancy.

In order to weight all arrays equally, we invoke a simple ranking scheme, where the grid point with the highest power in each window is assigned the rank of one, the grid point with the second highest power is assigned the rank of two, and so on. With this system, the ranks from individual arrays can be averaged at each grid point so that all arrays have equal weight. Figure 2b plots the same maximum powers as Figure 2a, but with the maximum average power replaced by the maximum average rank-power, showing that the rank-power average more equally balances contributions from all array stations. To combine the arrays for a single time window, we average the ranks from every point on the global grid first, and then consider the average values at only the grid points that are within joint coverage of all arrays.

To demonstrate that the ranking method is effective, we locate a known coherent event—a 5.2 M_w earthquake that occurred on January 3, 2010 in the Santa Cruz Islands. Figure 2c-e shows the maximum power and corresponding locations from a single array (ILAR), the averaged powers, and the averaged rank-powers. A single array suffers from a trade-off between distance and origin time. If the origin time is known, the event is well located by the single array, but if there is uncertainty in the origin time then only the azimuth is well constrained. Using the average of the array powers the event is properly located, but with a broader peak and greater uncertainty. The maximum average power also closely mirrors the single array power, once again showing the dominance of a single array with this method. The maximum average rank-power has a much smaller, tighter peak and identifies the event location well in space and time without being overly biased by a single array, demonstrating its effectiveness.

3.3 Source modeling

Frameworks for the modeling of microseismic energy generation in the double frequency band have been previously developed [*Longuet-Higgins*, 1950; *Hasselmann*, 1963; *Ardhuin et*

151 *al.*, 2011; *Ardhuin and Herbers*, 2013; *Traer and Gerstoft*, 2014]. In general, the two main
152 factors in the excitation of this energy are the effective pressure perturbation at the ocean surface
153 generated by wave-wave interactions, and an amplification coefficient that mediates the
154 translation of the ocean surface pressure into ground displacement. The ocean surface pressure
155 is a function of the wave frequency spectrum and the directional energy spectrum. Although
156 *Ardhuin et al.* [2011] point out that significant wave height does not have direct relationship with
157 seismic noise sources due to the absence of the directional energy component, we note that when
158 averaged over long periods of time, the sea state becomes uniform enough directionally and
159 spatially that the wave-wave interaction is essentially smoothed to an approximation of the
160 significant wave height [*Euler et al.*, 2014]. With this consideration in mind, we suggest that the
161 significant wave height is a reasonable approximation for the wave-wave interactions averaged
162 over an entire month for our high frequency band of interest (Figure 3a).

163 The amplification coefficient is primarily a function of frequency and water depth [e.g.,
164 *Longuet-Higgins*, 1950; *Ardhuin and Herbers*, 2013; *Gualtieri et al.*, 2014]. *Gualtieri et al.,*
165 [2014] demonstrated that this coefficient is distinct for body waves and surface waves, and we
166 use their P-wave formulation along with bathymetry and crustal velocities from Crust1.0 [*Laske*
167 *et al.*, 2013] to determine the values in our frequency range of interest (Figure 3b). Interestingly,
168 the high frequency coefficients are fairly uniform and much smoother geographically than those
169 for DF microseism frequencies (Figure 3c). Thus, we interpret our seismic energy back-
170 projection results mainly in terms of the significant wave height.

171

172 **4. Results**

We plot the back-projection results from individual arrays as maps of the average rank-powers and histograms of the maximum power locations in Figure 4. Average power maps are constructed by averaging the rank at each grid point over every window for the entire month of January 2010. Using the average ranks at individual arrays produces nearly identical results to maps constructed using median powers at each grid point, and is more computationally efficient given the number of time windows and grid points over which we average. This method is a way of de-emphasizing outliers, thus damping the effect of transient signals from earthquakes. Histograms are constructed by counting the number of times each grid point registered as a window's maximum power for all time windows in the month.

YKA and ILAR are situated near previously located lower-frequency DF miscroseism sources in the North Pacific (Figure 1) [e.g., *Landès et al.*, 2010; *Obrebski et al.*, 2013; *Zhang et al.*, 2010] and show great similarity in their results. Both exhibit strong energy to the southwest, with maximum powers most often concentrated in the north-central Pacific between ~38°–53°N latitude, overlapping areas of high significant wave height. YKA's maximum power locations are more diffuse and extend further to the west compared to those of ILAR, but this may be due in part to stronger slowness biases at ILAR [*Bondar et al.*, 1999]. Additionally, the YKA results exhibit strong power in the northern Atlantic, which is not apparent at ILAR, but again overlaps with high significant wave heights in the North Atlantic Ocean and is a region known to generate P-wave microseisms at longer DF periods [e.g., *Euler et al.*, 2014; *Landès et al.*, 2010; *Stutzmann et al.*, 2012].

The dominant energy at ASAR is to the south of the array and along the Southern Ocean, where significant wave heights in the southern hemisphere are the highest. Maximum powers are located most often very near the Great Australian Bight in the south central part of the

196 continent, which has previously been identified as a significant source of short-period seismic
197 noise in data recorded at the Warramunga Array (WRA) in north-central Australia [*Reading et*
198 *al.*, 2014]. The coupling of high significant wave heights and high amplification coefficients
199 near the coasts of Australia and Antarctica, suggests there is significant regional P-wave
200 microseism generation at this location and is in agreement with our observations.

201 Like ASAR, the results from KSRS display dominance from regional microseisms, where
202 maximum powers fall almost exclusively in the Sea of Japan. The consistency and longevity of
203 the power locations indicate this is an area of strong microseism generation. The strongest
204 average powers for KSRS are also mostly regional, but they extend to the east of Japan and, to a
205 lesser extent, along the north Pacific basin where the maximum powers of YKA and CMAR
206 locate. CMAR's strongest energy projects to the eastern portion of its coverage area,
207 overlapping much of the high power region displayed by ILAR and YKA. Substantial energy
208 also projects to portions of the Southern Ocean, in agreement with ASAR's locations of strongest
209 power. Maximum powers at CMAR most often plot in the south Pacific near the Philippines and
210 Indonesia, another likely area of regional microseism generation. However, the hit count for
211 CMAR is lower than at most of the other arrays indicating that the maximum power locations
212 occur frequently throughout a wide area of the Pacific.

213 When the rank-powers from all five arrays are combined, strong energy covers the
214 northern Pacific basin from approximately 15°–45°N latitude (Figure 5a), consistent with the
215 locations of the highest significant wave heights during the same time period (Figure 3a). We
216 observe very little energy on the Asian landmass, reinforcing the idea that transient signals from
217 earthquakes are not biasing our results. The locations with strongest energy are shown by the
218 histogram in Figure 5b. The maximum energy is concentrated in a smaller area from ~30°–45°N

219 latitude and ~180°–200°E longitude. We note that using subsets of only 3 arrays yields similar
220 results. Averaging ranks from ASAR, KSRS, and CMAR, for example, still yields strong energy
221 in the northern Pacific with roughly the same location as the strongest energy exhibited by all
222 five arrays, despite the fact that this energy is less dominant at any one of these arrays
223 individually. Because excluding any one or two arrays does not dramatically increase the
224 coverage area in the Pacific, and a better location is obtained with more stations, we include here
225 only the results from the combination of all five arrays.
226
227 **5. Discussion and Conclusions**
228 The strong high-frequency P-wave microseism source in the North Pacific Ocean that we
229 detect from the combined arrays shows good agreement with the study by *Koper et al.* [2010]
230 that overlapped backazimuth directions from three arrays to triangulate a source location for their
231 observed P-wave energy. Although they used a simpler methodology, we see a similar area of
232 maximum energy generation. Our results are also in good agreement with P-wave sources seen
233 at lower, DF, frequencies using larger aperture arrays [*Gerstoft et al.*, 2008; *Landès et al.*, 2010;
234 *Zhang et al.*, 2010], and, as Figure 5 shows, individual P-wave noise sources that have been
235 located and found to follow storm tracks in the Pacific Ocean [*Obrebski et al.*, 2013]. The broad
236 region of high energy that we see and the relative uniformity of the amplification coefficients at
237 higher frequencies (Figure 3) suggest that the areas over which high frequency microseisms are
238 generated may be more diffuse than at lower frequencies.
239 The strong regional P-wave microseism observations at ASAR and KSRS are similar to
240 work by *Zhang et al.* [2009], which found that the high-frequency body wave microseisms they
241 observed were correlated to nearby offshore wind speed. Others have also noted that at

242 frequencies above 0.2 Hz, strong correlations exist between microseismic energy and local wind
243 profiles [e.g., *Bromirski et al.*, 2005; *Hillers and Ben-Zion*, 2011], and due to short path lengths
244 and less attenuation, this energy may comprise a significant component of the microseism
245 spectra at coastal arrays. However, the ability to elucidate the North Pacific source using
246 multiple arrays at large distances suggests that this source may be the site of stronger microseism
247 generation than any of the regional locations. The dominance of the Northern Pacific source at
248 ILAR over nearby likely locations of regional energy also supports the conclusion that the North
249 Pacific source is very powerful.

250 Despite the dominant power in the DF microseismic band between 0.1–0.3 Hz, there is a
251 clear component of persistent, coherent P-wave microseismic energy in the higher (0.67–1.33
252 Hz) frequency band. The location in the North Pacific Ocean that we find from the rank
253 combination method shows striking similarity to the locations of lower-frequency sources, and
254 interestingly, even very long period surface waves from the Earth's hum [*Rhie and Romanowicz*,
255 2006]. Both high- and low-frequency sources are adequately explained by the mechanism
256 proposed by *Longuet-Higgins* [1950], and extended to shorter periods by *Webb and Cox* [1986],
257 suggesting that wave-wave interactions are a significant source of seismic energy that is quite
258 broadband in nature.
259

Acknowledgments

Seismic data from ASAR, ILAR, and YKA are freely available through the IRIS DMC. Data from CMAR and KSRS are from the NEIC and international agreements prohibit their public release. Data for Figure 3a are available from the IFREMER (French Research Institute for Exploitation of the Sea) ftp site (http://tinyurl.com/iowagaftp/iowaga/SISMO). This research was supported by the US National Science Foundation under grants EAR-0848132 and EAR-0951558. Additional work was performed at Lawrence Livermore National Laboratory under award number DE-AC52-06NA25946 and at Los Alamos National Laboratory under DE-AC52-06NA25396. Figures were made using Generic Mapping Tools (GMT) [*Wessel and Smith*, 1991].

Prepared by LLNL under Contract DE-AC52-07NA27344

References

Ardhuin, F., E. Stutzmann, M. Schimmel, and A. Mangeney (2011), Ocean wave sources of seismic noise, *J. Geophys. Res.*, *116*, C09004, doi:10.1029/2011JC006952.

Ardhuin, F., and T. H. C. Herbers (2013), Noise generation in the solid Earth, oceans and atmosphere, from nonlinear interacting surface gravity waves in finite depth, *J. Fluid. Mech.*, *716*, 316-348, doi:10.1017/jfm.2012.548.

Aster, R. C., D. E. McNamara, and P. D. Bromirski (2008), Multidecadal climate-induced variability in microseisms, *Seismol. Res. Lett.*, *79*(2), 194-202, doi:10.1785/gssrl.79.2.194.

Bondar, I., R. G. North, and G. Beall (1999), Teleseismic slowness-azimuth station corrections for the International Monitoring System seismic network, *Bull. Seismol. Soc. Am.*, *89*, 989-1003.

Boué, P., P. Poli, M. Campillo, and P. Roux (2014), Reverberations, coda waves and ambient noise: Correlations at the global scale and retrieval of the deep phases, *Earth Planet. Sci. Lett.*, *391*, 137-145, doi:10.1016/j.epsl.2014.01.047.

Brenguier, F., M. Campillo, C. Hadziioannou, N. M. Shapiro, R. M. Nadeau, and E. Larose (2008), Postseismic relaxation along the San Andres Fault at Parkfield from continuous seismological observations, *Science*, *321*, 1478-1481, doi:10.1126/science.1160943.

Bromirski, P. D., F. K. Duennebier, and R. A. Stephen (2005), Mid-ocean microseisms, *Geochem. Geophys. Geosyst.*, *6*(4), Q04009, doi:10.1029/2004GC000768.

Denolle, M. A., E. M. Dunham, G. A. Prieto, and G. C. Beroza (2013), Ground motion prediction of realistic earthquake sources using the ambient seismic field, *J. Geophys. Res. Solid Earth*, *118*, doi:10.1029/2912JB009603.

293 Ebeling, C. W. (2012), Inferring ocean storm characteristics from ambient seismic noise: A
294 historical perspective, *Adv. Geophys., 53*, 1-33.
295 Euler, G. G., D. A. Wiens, and A. A. Nyblade (2014), Evidence for bathymetric control on the
296 distribution of body wave microseism sources from temporary seismic arrays in Africa,
297 *Geophys. J. Int.*, *197*, 1869-1883, doi:10.1093/gji/ggu105.
298 Gerstoft, P., M. C. Fehler, and K. G. Sabra (2006), When Katrina hit California, *Geophys. Res.*
299 *Lett.*, *33*, L17308, doi:10.1029/2006GL027270.
300 Gerstoft, P., P. M. Shearer, N. Harmon, and J. Zhang (2008), Global P, PP, and PKP wave
301 microseisms observed from distant storms, *Geophys. Res. Lett.*, *35*, L23306,
302 doi:10.1029/2008GL036111.
303 Gualtieri, L., E. Stutzmann, V. Farra, Y. Capdeville, M. Schimmel, F. Ardhuin, and A. Morelli
304 (2014), Modelling the ocean site effect on seismic noise body waves, *Geophys. J. Int.*,
305 197(2), 1096-1106, doi:10.1093/gji/ggu042
306 Hasselmann, K. (1963), A statistical analysis of the generation of microseisms, *Rev. Geophys.*,
307 *1*(2), 177-210.
308 Haubrich, F. A., and K. McCamy (1969), Microseisms: coastal and pelagic sources, *Rev.*
309 *Geophys.*, *7*(3), 539-571.
310 Hillers, G. and Y. Ben-Zion (2011), Seasonal variations of observed noise amplitudes at 2-18 Hz
311 in southern California, *Geophys. J. Int.*, *184*(2), 860-868, doi:10.1111/j.1365-
312 246X.2010.04886.x
313 Kennett, B. L., E. R. Engdahl, and R. Buland (1995), Constraints on seismic velocities in the
314 Earth from travel times, *Geophys. J. Int.*, *122*, 108-124.

315 Koper, K. D., and B. de Foy (2008), Seasonal anisotropy in short-period seismic noise recorded
316 in South Asia, *Bull. Seismol. Soc. Am.*, *98*(6), 3033-3045, doi:10.1785/0120080082.
317 Koper, K. D., K. Seats, and H. Benz (2010), On the composition of Earth's short-period seismic
318 noise field, *Bull. Seismol. Soc. Am.*, *100*(2), 606-617, doi:10.1785/0120090120.
319 Landès, M., F. Hubans, N. M. Shapiro, A. Paul, and M. Campillo (2010), Origin of deep ocean
320 microseisms by using teleseismic body waves, *J. Geophys. Res.*, *115*, B05302,
321 doi:10.1029/2009JB006918.
322 Laske, G., G. Masters, Z. Ma, and M. Pasayanos (2013), Update on CRUST1.0: a 1-degree
323 global model of Earth's crust, *Geophys. Res. Abstr.*, *15*, Abstract EGU2013-2658.
324 Lawrence, J. F., and G. A. Prieto (2011), Attenuation tomography of the Western United States
325 from ambient seismic noise, *J. Geophys. Res.*, *116*, B06302, doi:10.1029/2010JB007836.
326 Longuet-Higgins, M. S. (1950), A theory of the origin of microseisms, *Phil. Trans. R. Soc. Lond.*
327 *A*, *243*(857), 1-35.
328 Muirhead, K. J., and R. Datt (1976), The Nth root process applied to seismic array data,
329 *Geophys. J. R. Astr. Soc.*, *47*, 197-210.
330 Obrebski, M., F. Ardhuin, E. Stutzmann, and M. Schimmel (2013), Detection of microseismic
331 compressional (P) body waves aided by numerical modeling of oceanic noise sources, *J.*
332 *Geophys. Res. Solid Earth*, *118*, doi:10.1002/jgrb.50233.
333 Poli, P., M. Campillo, H. Pedersen, and LAPNET Working Group (2012), Body-wave imaging
334 of Earth's mantle discontinuities from ambient seismic noise, *Science*, *338*(6110), 1063-
335 1065, doi:10.1126/science.1228194.
336 Reading, A. M., K. D. Koper, M. Gal, L. S. Graham, H. Tkalčić, and M. A. Hemer (2014),
337 Dominant seismic noise sources in the Southern Ocean and West Pacific, 2000-2012,

recorded at the Warramunga Seismic Array, Australia, *Geophys. Res. Lett.*, *41*, doi:10.1002/2014GL060073.

Rhie, J. and B. Romanowicz (2006), A study of the relation between ocean storms and the Earth's hum, *Geochem, Geophys, Geosyst.*, *7*, Q10004, doi:10.1029/2006GC001274.

Roux, P., K. G. Sabra, P. Gerstoft, and W. A. Kuperman, (2005), P-waves from cross-correlation of seismic noise, *Geophys. Res. Lett.*, *32*, L19303, doi:10.1029/2005GL023803.

Shapiro, N. M., M. Campillo, L. Stehly, and M. H. Ritzwoller (2005), High-resolution surface-wave tomography from ambient seismic noise, *Science*, *307*, 1615-1618.

Stutzmann, E., F. Ardhuin, M. Schimmel, A. Mangeney, and G. Patau (2012), Modeling long-term seismic noise in various environments, *Geophys. J. Int.*, doi:10.1111/j.1365-246X.2012.05638.x

Toksöz, M. N., and R. T. Lacoss (1968), Microseisms: Mode structure and sources, *Science*, *159*, 872-873.

Tolman, H. L. (2008), A mosaic approach to wind wave modeling, *Ocean Modell.*, *25*, 35-47.

Traer, J. and P. Gerstoft (2014), A unified theory of microseisms and hum, *J. Geophys. Res. Solid Earth*, *119*, doi:10.1002/2013JB010504.

Webb, S. C., and C. S. Cox (1986), Observations and modeling of seafloor microseisms, *J. Geophys. Res., 91*, 7343-7358.

Wessel, P., and W. H. F. Smith (1991), Free software helps map and display data, *EOS Trans. AGU*, *72*, 441, 445-446, doi:10.1029/90EO00319.

Xu, Y., K. D. Koper, O. Sufri, L. Zhu, and A. R. Hutko (2009), Rupture imaging of the M_w 7.9 12 May 2008 Wenchuan earthquake from back projection of teleseismic P waves, *Geochem. Geophys. Geosyst.*, *10*, Q04006, doi:10.1029/2008GC002335.

Zhang, J., P. Gerstoft, and P. M. Shearer (2009), High-frequency P-wave seismic noise driven by ocean winds, *Geophys. Res. Lett.*, *36*, L09302, doi:10.1029/2009GL037761.

Zhang, J., P. Gerstoft, and P. D. Bromirski (2010), Pelagic and coastal sources of P-wave microseisms: Generation under tropical cyclones, *Geophys. Res. Lett.*, *37*, L15301, doi:10.1029/2010GL044288.

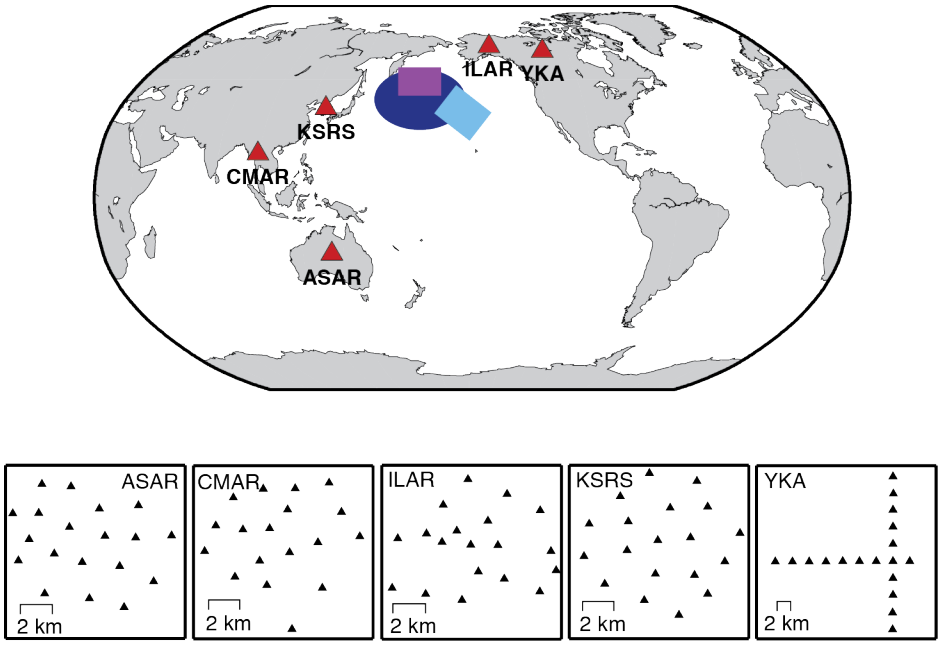

367

368

369 **Figure 1.** Location of IMS arrays used in this study. Bottom panels show individual array
370 configurations. Colored symbols show locations of previous DF microseism generation
371 locations in the North Pacific. Dark blue patch is from *Zhang et al.* [2010] (their Figure 4a),
372 purple is from *Landès et al.* [2010] (Figure 9b), and light blue is from *Koper et al.* [2010] (Figure
373 8).

374

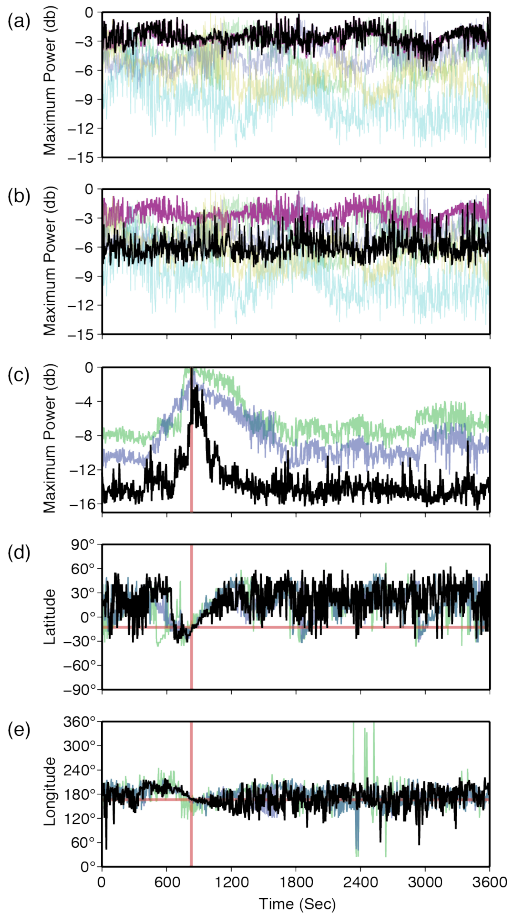

375

376

377 **Figure 2.** Comparison of array combination from power averaging versus rank-power
378 averaging. (a) Individual array powers and averaged power (black) for a quiet hour with no
379 earthquakes on January 6, 2010, 08:00. (b) Same as (a) but with the rank-power average plotted
380 in black. In (a) and (b) the individual array station ILAR is plotted in purple. (c) Comparison of
381 rank-power average (black) to power average (blue) and power from ILAR (green) for a 5.2 M_w
382 event in the Santa Cruz Islands on January 3, 2010, 15:13. Latitude and longitude associated
383 with each power measurement are plotted in (d) and (e) respectively. Red lines show time and
384 location of the event, as reported in the NEIC PDE catalog. The rank-power average removes
385 dominance by a single array while still providing excellent locations in space and time.

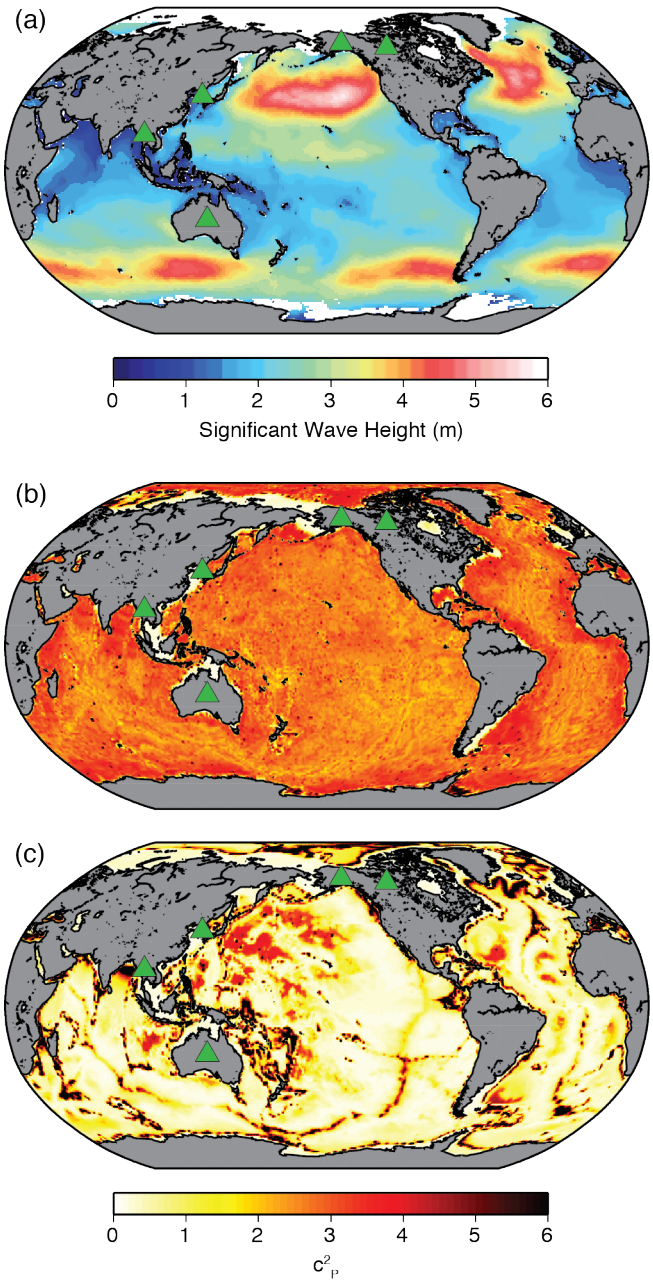

386

387

388 **Figure 3.** (a) Map of the median significant wave height for the month of January 2010 based

389 on the WAVEWATCH III® model [*Tolman*, 2008]. (b) and (c) Average P-wave amplification

390 coefficients [*Gualtieri et al.*, 2014] at frequencies of (b) 0.67–1.33 Hz, and (c) 0.135–0.2 Hz.

391

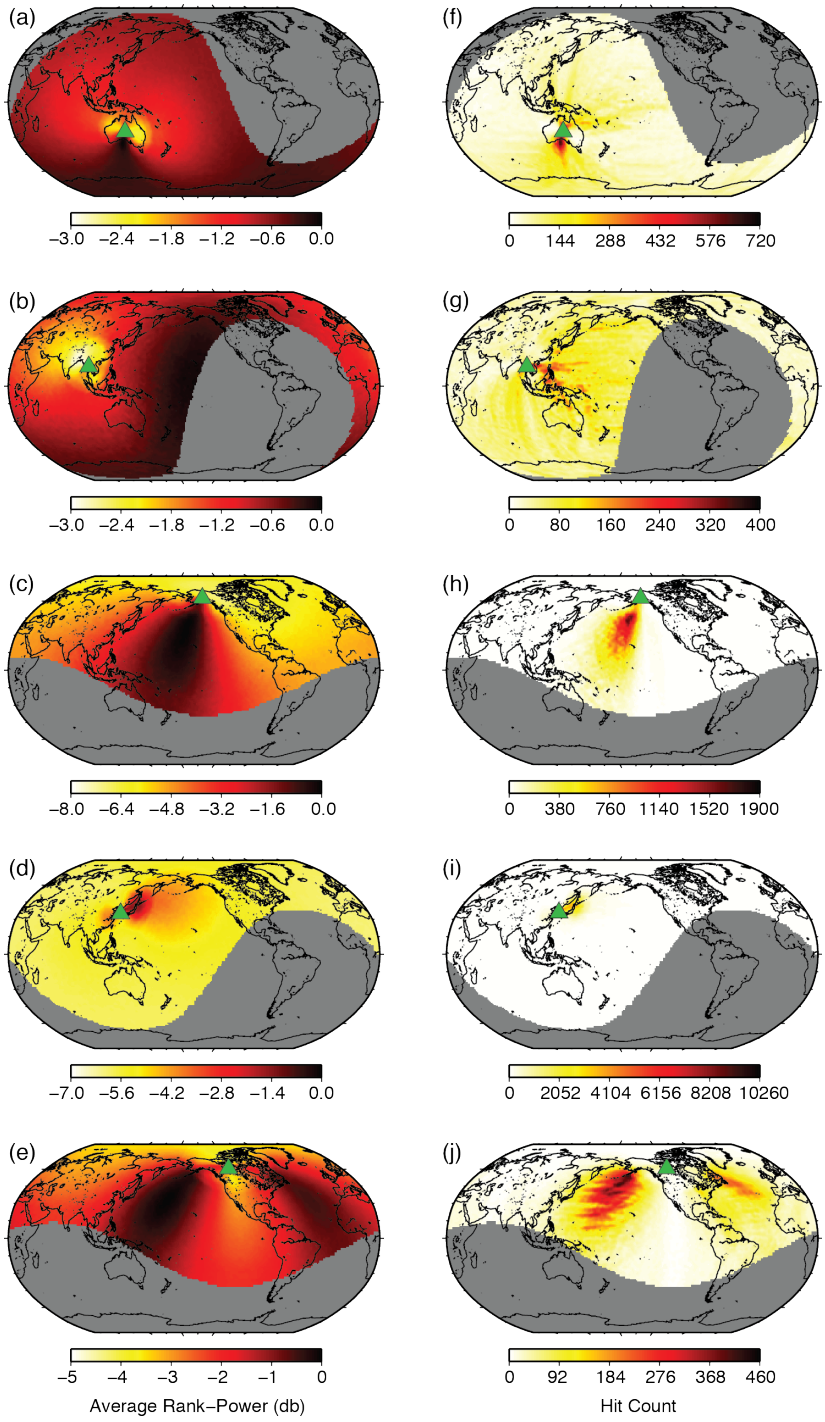

392

393

394 **Figure 4.** Average rank-power maps and histograms of maximum powers for individual arrays.

395 (a) and (f) are the average rank-power map and histogram, respectively, for ASAR, (b) and (g)

396 are the maps for CMAR, (c) and (h) ILAR, (d) and (i) KSRS, and (e) and (j) YKA.

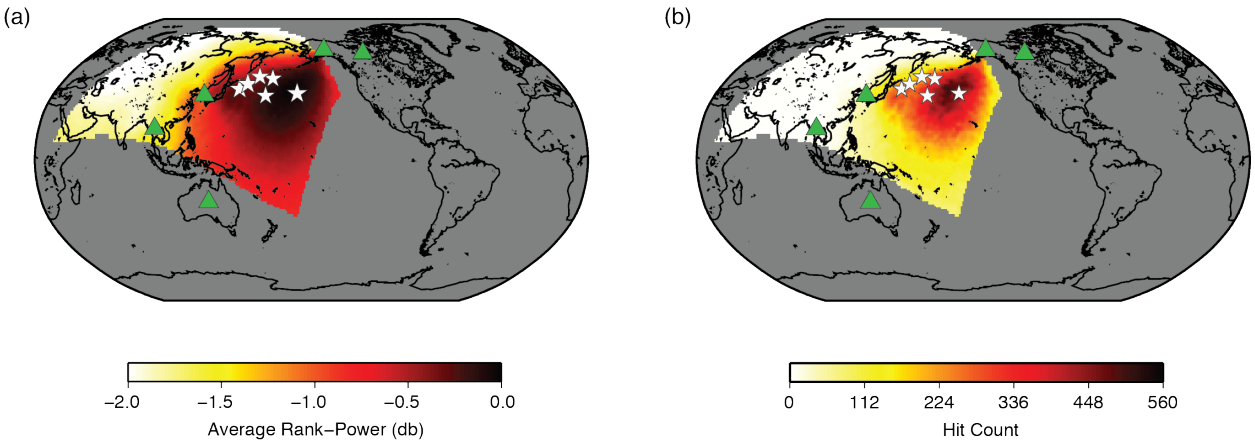

397

398

399 **Figure 5.** (a) Average rank-power and (b) maximum power histogram maps for the combination

400 of all five arrays. Combination of arrays is performed using the ranking scheme described in the

401 text. White stars mark the locations of noise sources in the double-frequency band (0.193 Hz)

402 located during the same time period, January 2010, by *Obrebski et al.* [2013].

403